ACS APPLIED MATERIALS & INTERFACES

RESEARCH ARTICLE

www.acsami.org

Fabrication and Temperature-Dependent Field-Emission Properties of Bundlelike VO_2 Nanostructures

Haihong Yin,[†] Min Luo,[†] Ke Yu,[*,†] Yanfeng Gao,[‡] Rong Huang,[†] Zhengli Zhang,[†] Min Zeng,[†] Chuanxiang Cao,[‡] and Ziqiang Zhu[†]

[†]Key Laboratory of Polar Materials and Devices (Ministry of Education of China), Department of Electronic Engineering, East China Normal University, Shanghai 200241, China

[‡]Research Center for Industrial Ceramics, Shanghai Institute of Ceramics, Chinese Academy of Sciences, Dingxi 1295, Changning, Shanghai, 200050, China

ABSTRACT: Bundlelike $VO_2(B)$ nanostructures were synthesized via a hydrothermal method, and $VO_2(M_1/R)$ nanobundles were obtained after a heat-treatment process. Structural characterization shows that these nanobundles are self-assembled by VO_2 nanowires, and $VO_2(M_1/R)$ nanobundles have better crystallinity. Temperature-dependent field-emission (FE) measurement indicates that FE properties of these two phases of nanobundles can both be improved by increasing the ambient temperature. Moreover, for the $VO_2(M_1/R)$ nanobundles, their FE properties are also strongly dependent on the temperature-induced metal−insulator transitions process. Compared with poor FE properties found in the insulating phase, FE properties were significantly improved by increasing the temperature, and about a three-orders-of-magnitude increasing of the emission current density has been observed at a fixed field of 6 V/μm. Work function measurement and density-functional theory calculations indicated that the decrease of work function with temperature is the main reason that caused the improvement of FE properties. These characteristics make $VO_2(M_1/R)$ a candidate material for application of new type of temperature-controlled field emitters, whose emission density can be adjusted by ambient temperature.

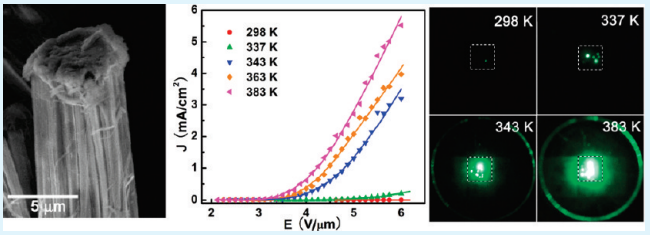

KEYWORDS: vanadium dioxide, field emission, density of states

1. INTRODUCTION

One-dimensional (1D) nanostructures such as nanotubes, nanowires, and nanorods have stimulated much attention for their potential application in optoelectronic devices because of their favorable properties. Since the discovery of the excellent field-emission (FE) properties of carbon nanotubes,[1,2] intensive research on electron emission of ZnO,[3−5] SnO_2,[6] In_2O_3,[7] CuO,[8] TiO_2,[9] MnO_2,[10] tungsten oxides,[11,12] and other metal oxide nanostructures have been performed because of their potential application in back-lighting, field-emission display, X-ray source, and amplifier.

Among various metal oxides nanomaterials, vanadium dioxide (VO_2) nanostructures have attracted great attention because of their different polymorphs and special optical, electrical, and magnetic properties. The allotropic phases in VO_2 system include $VO_2(R)$, $VO_2(M_1)$, $VO_2(B)$, $VO_2(A)$,[13] and recently reported $VO_2(C)$.[14] When heated to 340 K, $VO_2(M_1)$ will show a reversible first-order metal−insulator transition (MIT). The transition is characterized by a structural phase transformation from high-temperature metallic tetragonal phase ($P4_2/mnm$, R phase) to low-temperature insulating monoclinic phase ($P2_1/c$, M_1 phase),[15] which corresponds to V^{4+} cations along the rutile c axis, forming homopolar bonds, and undergoing a structural twist. The resistivity jumps by several orders of magnitude through the process of phase transition, and the optical transmittance abruptly decreases in the near-IR region. These properties of VO_2 make it a promising material for the applications in nanoscale devices such as bolometers,[16] memristors[17] and memory metamaterials.[18] $VO_2(B)$, one of the metallic phases of vanadium dioxide, is of great interest because of its layered structure and promising properties in the nanometer regime.[19−22] It is an attractive material for various applications, especially as an electrode material for lithium batteries.[20] $VO_2(B)$ exhibits a maximum reversible capacity of about 320 mA h g^{-1} in the range of 4 to 1 V in lithium cells.[20,22]

Despite these attractive features and many efforts on the application of VO_2, there have been few reports on the FE properties of VO_2 nanostructures. Wang and Zhang first reported the electron emission from VO_2 nanorods; however, these VO_2 nanorods synthesized by them are not in B or M_1/R phases but in a new body-centered-cubic structure that has never been observed before.[23] For M_1/R phase nanostructures, because of the drastic resistivity change through MIT and different work function of these two phases, FE properties should be

Received: March 8, 2011
Accepted: May 23, 2011
Published: June 02, 2011

different and strongly dependent on the ambient temperature. Knowledge of their FE properties is essential for their potential application in new generation of temperature-controlled electron emitters. In this work, massive bundlelike VO_2(B) nanostructures were first synthesized, and VO_2(M_1/R) nanobundles were then obtained by heating VO_2(B) in an inert atmosphere. Temperature-dependent FE emission properties of both two types of the nanobundles were investigated, respectively. It is demonstrated that their FE properties can both be improved by increasing the ambient temperature. Moreover, FE properties of VO_2(M_1/R) nanobundles are also strongly dependent on the MIT process, and about a three-orders-of-magnitude increasing of the emission current density has been observed. These characteristics make VO_2 a candidate material for new generation of temperature-controlled field emitters.

2. EXPERIMENTAL METHODS

Synthesis of VO_2 Nanobundles. VO_2(B) nanobundles were synthesized by a hydrothermal procedure. 0.36 g of commercial V_2O_5 powder was added to 80 mL oxalic acid (0.1 mol/L) in aqueous solution to form yellow slurry. The slurry was stirred for 20 min and then transferred to a 100 mL autoclave with a Teflon linear. The autoclave was maintained at 180 °C for four days and then air-cooled to room temperature. The resulting dark blue precipitates (VO_2(B)) were collected and washed with distilled water and ethanol several times and then dried at 60 °C under vacuum for 10 h. At last, VO_2(M_1/R) powders were obtained by heating VO_2(B) at 650 °C in an argon atmosphere for 1 h. In all reactions, the content of the commercial V_2O_5 powder is kept unchanged.

Characterization. The synthesized VO_2(B) and VO_2(M_1/R) powders were screen-printed on metal copper substrates, and the obtained B and M_1/R phase VO_2 films were used for characterization. The morphology and structure of the samples were characterized by field emission scanning electron microscopy (FESEM, JEOL-JSM-6700F), X-ray diffraction (XRD, D/MAX 2550 V) with Cu Kα radiation and transmission electron microscopy (TEM, Philips Tecnai 20U-TWIN). Differential scanning calorimetry (DSC DSC204F1, NETZSCH) experiments were performed in nitrogen flow in the range from 303 to 358 K with a heating rate of 1 K/min.

Field-Emission Measurement. For field emission investigation, the synthesized VO_2(B) and VO_2(M_1/R) nanobundles were painted on the metal copper substrates by a screen-printing method, respectively. The copper substrate with nanomaterial (as a cathode) was separated from a phosphor/indium tin oxide (ITO)/glass anode by two Teflon spacers with a thickness of 200 μm. FE properties were measured with a high vacuum level of about 5×10^{-5} Pa at different temperatures using transparent anode imaging technique. The measured emission area was 1×1 cm^2. In the measurement, the turn-on field is determined as the field needed to produce a current density of 0.1 μA/cm^2, and the threshold field is the field needed to produce a current density of 1 mA/cm^2.

3. RESULTS AND DISCUSSION

Representative SEM images of VO_2(B) nanobundles synthesized by hydrothermal method are shown in Figure 1A–C. Figure 1A shows that the products are composed of a large quantity of bundle-like nanostructures with lengths of about 40–50 μm. The middle- and high-magnification SEM images shown in B and C in Figure 1 indicate that these nanobundles have a diameter of about 5–10 μm, and are assembled by a large quantity of VO_2 nanowires having the same orientation. Peaks of the corresponding XRD pattern of these nanobundles

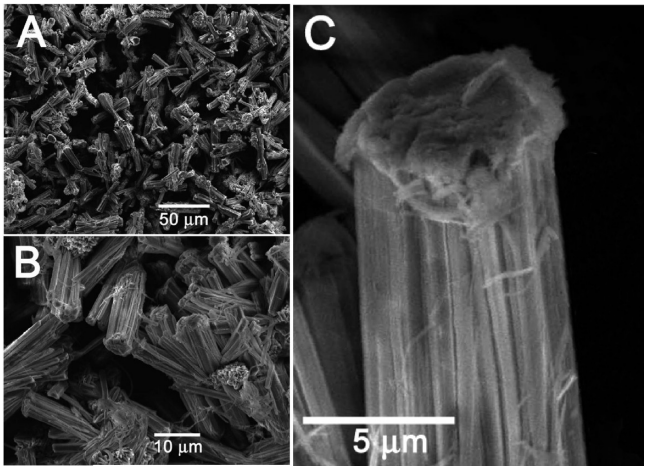

Figure 1. (A) Low-, (B) medium-, and (C) high-magnification SEM images of VO_2(B) nanobundles synthesized by hydrothermal method.

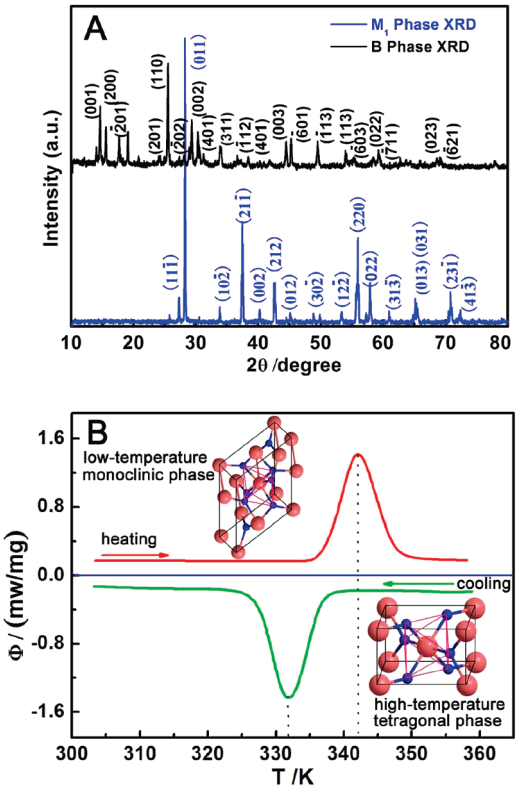

Figure 2. (A) XRD patterns of obtained VO_2 samples, B phase (black) and M_1 phase (blue). (B) DSC thermal spectra of as-obtained VO_2(M_1) nanobundles showing a narrow heating–cooling hysteresis and excellent MIT behavior between two thermodynamically stable structures. Upper inset (left), the low-temperature insulating M_1 structure. Lower inset (right), the high-temperature metallic R structure. Large red spheres, V atoms; small blue spheres, O atoms.

(Figure 2A, in black) are indexed to VO_2(B) phase (space group: C_2/m) with lattice constants of a = 12.03 Å, b = 3.693 Å, c = 6.42 Å, and β = 106.6° (JCPDS 31–1438). Despite some impurity peaks existing in the XRD pattern, the main peaks of VO_2(B) in the XRD pattern indicate the products are mostly composed of VO_2(B) nanostructures. Among many polymorphs

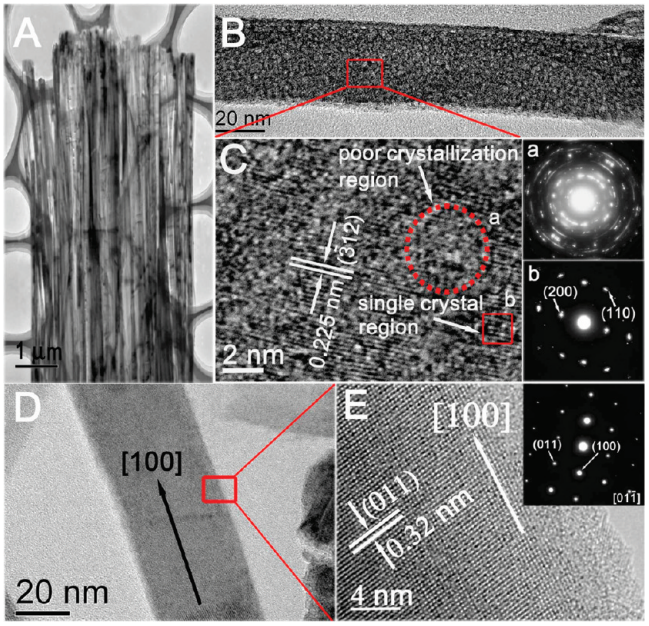

Figure 3. (A) Low-magnification TEM image of VO_2(B) nanobundles. (B) TEM image of a single VO_2(B) nanowire. (C) HRTEM image for the square region of panel B marked in red. Regions marked with red dash circle and red rectangle indicate coexistence of poor crystallization regions and single-crystal regions. (a) SAED patterns taken at the position of circle a (red dash circle) on the nanowire. (b) SAED patterns taken at the position of rectangle b. (D) TEM image of a single $VO_2(M_1)$ nanowire. (E) HRTEM image of the region marked with a red rectangle in panel D. Upper inset, the corresponding SAED pattern indexed using a $[01\bar{1}]$ zone axis.

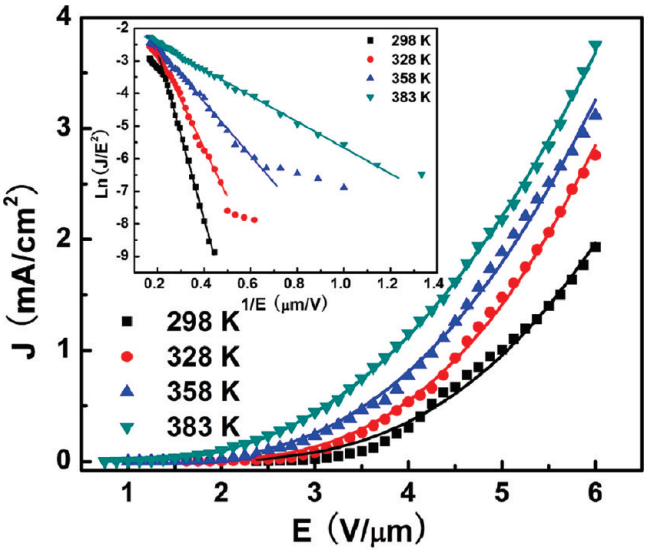

Figure 4. Dependence of the FE current density J on the applied electric field strength E of VO_2(B) nanobundles for different temperatures. Inset, the corresponding Fowler−Nordheim (F−N) plots.

of VO_2, only rutile-type $VO_2(M_1/R)$ undergoes first-order reversible metal−insulator transition between M_1 phase and R phase, and is usually synthesized by transforming VO_2(B) to $VO_2(M_1/R)$ at high temperatures. After heat-transformation, $VO_2(M_1)$ phase nanobundles were obtained, and the subsequent SEM research indicates that the nanostructure is still not destroyed. The XRD pattern (Figure 2A, in blue) indicates that all diffraction peaks are identical to those of monoclinic $VO_2(M_1)$ (space group: $P2_1/c$) according to JCPDS card 44−0252 with lattice constants of a = 5.753 Å, b = 4.526 Å, c = 5.383 Å, and β = 122.6°. No peaks of any other phases or impurities were detected in the spectra, revealing the high phase purity of $VO_2(M_1)$ products. To the best of our knowledge, this is the first time that bundlelike VO_2 nanostructures were obtained. The reversible transition characteristics between the M_1 and R phases were confirmed by differential scanning calorimetry (DSC) (Figure 2B) measurement, which shows a narrow heating−cooling hysteresis and an excellent MIT behavior.

Low-magnification TEM image of VO_2(B) nanobundles is shown in Figure 3A, indicating that these VO_2 nanowires, which self-assembled together and formed nanobundles, have nearly same diameters. Figure 3B presents a TEM image of a single VO_2(B) nanowire, clearly demonstrating that the diameters of these VO_2(B) nanowires are about 30−40 nm. High-resolution (HR) TEM image in Figure 3C demonstrates that the lattice spacing is 0.225 nm corresponding to the $(\bar{3}12)$ plane of VO_2(B). Interestingly, it can be seen from Figure 3B that there are a large number of mottles widely distributed in the VO_2(B) nanowire. Further high-resolution TEM (HRTEM) investigation indicates that these VO_2(B) nanowires have low crystallinity, and these mottles correspond to poor crystallization regions as marked by red dashed circle in Figure 3C. The selective area electron diffraction pattern (SAED) shown in Figure 3a, b was taken from different areas of a single nanowire. The different SAED results indicate that the single nanowire has different crystallinity: the red circle part is poor crystallization region; the red rectangle part is single-crystal region. Such a result confirmed the coexisting of poor crystallization regions and single crystal regions in the nanowire. For the $VO_2(M_1)$ samples, TEM investigation are also proceeded, and TEM and HRTEM images of a single $VO_2(M_1)$ nanowire are shown in D and E in Figure 3, respectively. In Figure 3D, it is noted that the mottles disappeared in the $VO_2(M_1)$ nanowire after the heat-transformation. The HRTEM image of Figure 3E shows that these $VO_2(M_1)$ nanowires have high crystallinity, and the disappearance of poor crystallization regions through the heat-transformation process caused the disappearance of these mottles. In the HRTEM image, the lattice spacing is 0.32 nm corresponding to the (011) plane of $VO_2(M_1)$. The SAED pattern (the inset of Figure 3E) indicates that these nanowires grew along the [100] direction with a zone axis of $[01\bar{1}]$. In the measurement, the diffraction pattern did not change as the electron beam moved along the nanowire, indicating that the whole nanowire is a single crystal.

Field-emission properties of $VO_2(M_1)$ and VO_2(B) samples were measured by the method mentioned at the Experimental Section. Figure 4 shows the relationship between the emission current density (J) and the applied electric field (E) for VO_2(B) nanobundles at temperatures of 298, 328, 358, and 383 K, respectively. The turn-on field decreased from 2.375 V/μm (at 298 K) to 0.8 V/μm (at 383 K), and the threshold field decreased from 5.09 V/μm (at 298 K) to 3.85 V/μm (at 383 K), indicating that the nanobundles at higher temperature exhibit larger current densities under the same applied field. The inset of Figure 4 is the corresponding Fowler-Nordheim (F−N) plots with $\ln(J/E^2)$ and $1/E$. These straight lines indicate that the emitting electrons mainly resulted from field emission.

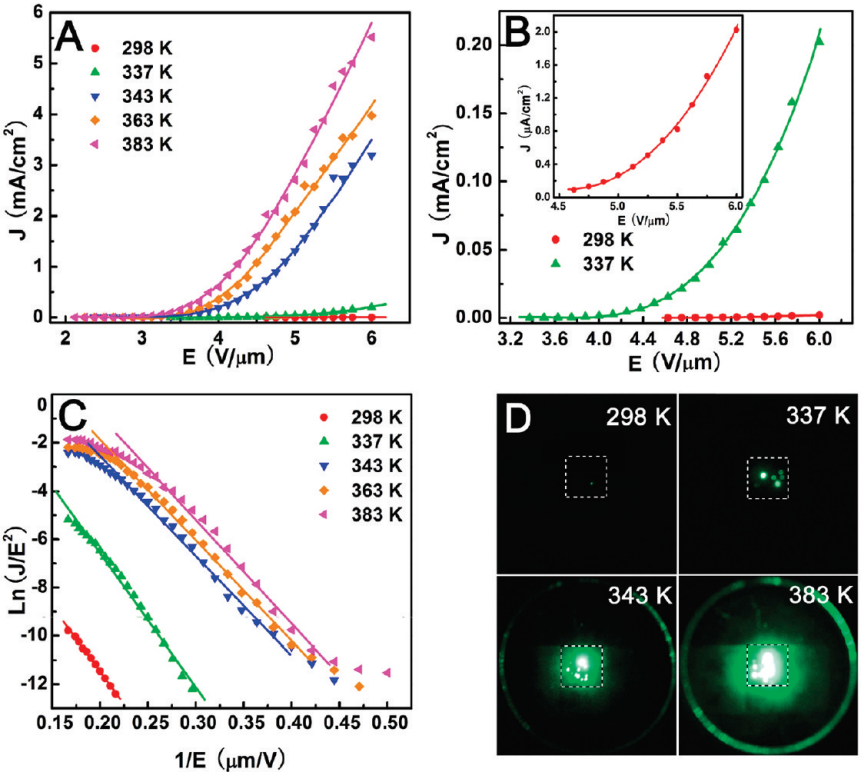

Figure 5. (A) Dependence of the FE current density J on the applied electric field strength E of $VO_2(M_1/R)$ nanobundles for different temperatures. (B) Expanded $J-E$ plot of $VO_2(M_1/R)$ nanowires at 298 and 343 K respectively. (C) Fowler−Nordheim relation of $\ln(J/E^2) - 1/E$ plots. (D) Electron emission images of the screen-printed $VO_2(M_1/R)$ nanostructures at 298, 337, 343, and 383 K for an applied field 6 V/μm, respectively.

Considering the MIT characteristic of $VO_2(M_1/R)$ nanobundles, their temperature-dependent field emission properties should be quite different from that of $VO_2(B)$ and many other metal oxides,[8,24] thus we pay more attention to investigate the temperature dependence of field-emission properties of VO_2-(M_1/R) nanobundles. Figure 5A shows typical plots of FE current density versus applied field ($J-E$) of $VO_2(M_1/R)$ nanobundles at different temperature from 298 to 383 K. The expanded view of the $J-E$ characteristic at 298 and 337 K are shown in Figure 5B. It is visible that the emission current density J increases exponentially with the applied field E, and the FE properties can be obviously improved by increasing the temperature. For the ambient temperature of 298, 337, 343, 363, and 383 K, the turn-on fields clearly decreased with the temperature, whose values are 4.65, 3.38, 2.45, 2.36, and 2.1 V/μm, respectively. In this process, the threshold electric fields also decreased with temperature. Their values at 343, 363, and 383 K are 4.80, 4.45, and 4.22 V/μm respectively. It is also found that the current density increases obviously with the temperature (Figure 5A). At 298 and 337 K, under the applied field of 6 V/μm, the film has weaker emission current density with maximum values of 2.01 and 202 μA/cm^2, respectively, as shown in Figure 5B. The maximum emission current density increased significantly when the temperature was higher than 343 K. Their values are 3.19, 3.97, and 5.51 mA/cm^2, corresponding to the temperature of 343, 363, and 383 K respectively. Figure 5D shows the real-time emission images of the $VO_2(M_1/R)$ samples at 298, 337, 343, and 383 K, respectively, recorded by CCD camera and tested at the applied field of 6 V/μm. It can be seen clearly that the emitting intensity increases with the temperature increasing from 298 to 383 K. At 298 and 337 K, in the insulating (M_1) phase, few emitting spots were observed and the brightness is very low because the threshold fields of the $VO_2(M_1)$ nanobundle emitter are larger than 6 V/μm at both temperatures. At 343 and 383 K, in the metallic (R) phase, the number of emission spots increased significantly and the emission spots density is estimated to be about 1×10^3 and 1×10^4 cm^{-2}, respectively. Here, the emission current may come from both field emission and thermionic emission. However, the thermionic emission current should be very weak.[8] Therefore we believe that this phenomenon may be strongly related to the properties of VO_2 MIT process, and it should be the work function change in the MIT process of $VO_2(M_1/R)$ that caused the observed dramatic increase in emission current density.

To confirm the interpretation that it was the work function change in the MIT process that caused the improvement of field emission, the temperature dependent work function of these $VO_2(M_1/R)$ nanobundles was investigated by UPS analysis. Figure 6 shows the corresponding UPS spectra at different temperature, which were obtained by a Shimadzu Axis Ultra electron spectrometer using He (I) ultraviolet light (21.22 eV) as the excitation source. It can be seen clearly from Figure 6 that the work function decreases when the temperature increases. Their values at 298 and 353 K are ~4.10 and ~3.65 eV, as shown in the inset of Figure 6, corresponding to M_1 phase and R phase, respectively. For M_1 phase, from 298 to 333 K, as can be seen from the inset of Figure 6, the decrease of the work function is about 0.07 eV. For R phase, about a 0.02 eV decrease in the work function was observed from 343 to 383 K. In the near region of 340 K, the MIT process will happen, and the work function

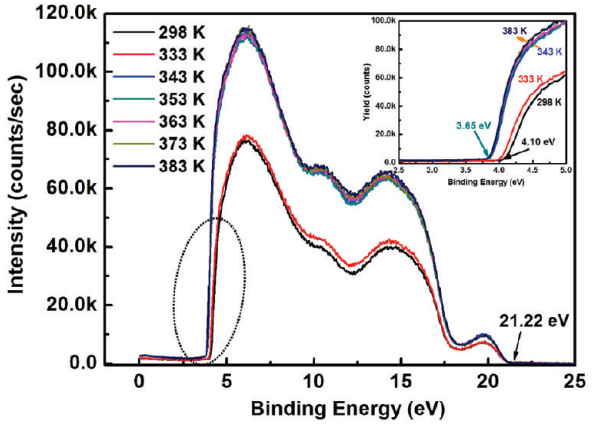

Figure 6. Temperature-dependent UPS spectra of the $VO_2(M_1/R)$ nanobundles. Inset shows an expanded view for the region marked in dotted eclipse.

decrease of ~0.4 eV (from 333 to 343 K) was observed from Figure 6. Therefore, the work function decrease will cause the improvement of FE properties of $VO_2(M_1/R)$ nanobundles.

The Fowler−Nordheim (F−N) plots are shown in Figure 5C. These straight lines indicate that the emitting electrons are mainly resulted from field emission. The behavior of the emission current versus the applied voltage was analyzed using the Fowler−Nordheim equation

$$J = A\frac{\beta^2 E^2}{\phi}\exp\left(-\frac{B\phi^{3/2}}{\beta E}\right) \quad (1)$$

where $A = 1.54 \times 10^{-6}$ A eV V^{-2}, $B = 6.83 \times 10^9$ $eV^{-3/2}$ V m^{-1}, β is the field enhancement factor, and ϕ is the work function of the emitter material. Here, the work function of M_1 and R phase VO_2 nanobundles were ~4.10 and ~3.65 eV, respectively. Therefore, the estimated field enhancement factors lie in the range 1020−1400, indicating large field-enhancement factors of synthesized $VO_2(M_1/R)$ nanobundles.

To explain the influence of the temperature on work function changes of $VO_2(M_1/R)$, we studied electrons' density of states (DOS) of monoclinic and tetragonal phases under several different temperatures through first-principles theory calculations. The calculations are performed at the level of density functional theory (DFT), using the PW91 generalized gradient approximation (GGA) and the projector augmented wave (PAW) method, as implemented in the Vienna ab initio simulation package (VASP). In our calculation, $U = 4.2$ eV and $J = 0.8$ eV were used to describe the electron exchange-correlation interaction,[25,26] and the obtained DOS were shown in Figure 7. In the insulating phase, the dimerization and the off-axis zigzag displacement of V−V pairs lead to a band splitting with the formation of a Peierls-like gap at the Fermi level.[27] The band gap is thus determined by the localized charge variation, which depends on changes in V−V pair twist and varies sensitively with the separation of V−V pairs along the c axis. When the temperature increases to around 340 K, the MIT process happens, VO_2 transforms from monoclinic structure to tetragonal structure, therefore the gap will become narrower (Figure 7A). In our calculations, the obtained band gap at 298 K is about 0.58 eV, agreeing with optical data and previous calculation results,[28,29] and its value decreased to 0.46 eV when

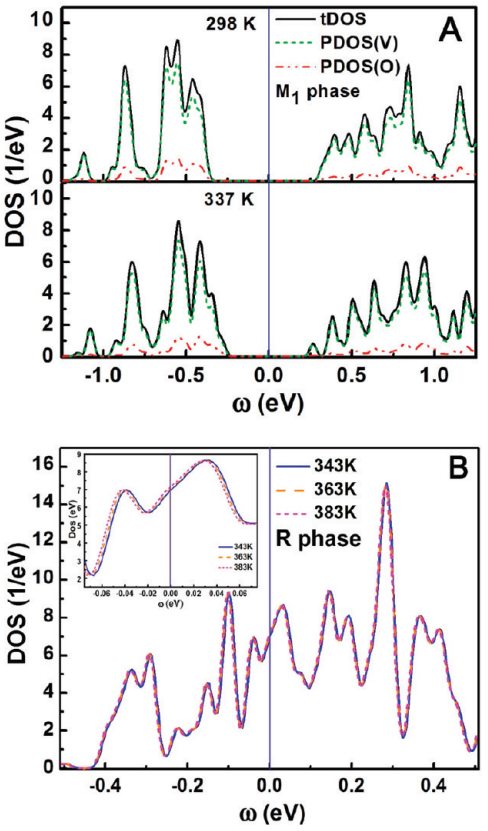

Figure 7. DOS of the $VO_2(M_1/R)$ at (A) 298 and 337 K, and (B) 343, 363, and 383 K calculated using the density-functional theory method. Inset shows an expanded view for DOS of R phase.

the temperature increases to 337 K, as shown in Figure 7A. The decrease of the gap value (0.12 eV) must lead to the decrease of the work function, and thus cause the significant improvement of the FE properties of $VO_2(M_1)$. Our calculation results show good agreement with the work function measurement that a ~0.07 eV decrease (Figure 6) of the work function was observed from 298 to 333 K, and it can be confirmed by the FE measurement (Figure 5B) that the maximum current density at 337 K is about 100 times of that at 298 K. And these DOS calculation results are also consistent with the recent report of Yao.[26] When the temperature increased to 343 K, the MIT process was completed, VO_2 nanomaterials were in tetragonal phase, therefore the disappearance of the gap and the drastic increase of the conductivity caused the further decrease of work function (Figure 6) and caused significant improvement of the FE properties (Figure 5A). In the metallic phase, with the temperature increasing higher, the maximum current density of $VO_2(R)$ kept on increasing, but at a lower rate. This phenomenon is mainly due to the work function decrease caused by the upward shift of Fermi level with temperature increasing. In the inset of Figure 7(B), the DOS of $VO_2(R)$ clearly indicates a tiny upward shift (about 1.6 meV) of the Fermi level with the temperature increasing from 343 to 383 K. Moreover, the upward shift of Fermi level in metallic phase is far less than the change of gap in insulating phase. Thus, the work function decrease of $VO_2(R)$ is far less than that of $VO_2(M_1)$, which were confirmed by the work function measurement in Figure 6, and should be the reason why the temperature has a more strong

influence on the FE properties for $VO_2(M_1)$ phase than for $VO_2(R)$ phase, as shown in Figure 5.

4. CONCLUSIONS

In summary, bundlelike B phase VO_2 nanomaterials have been synthesized by hydrothermal procedure, and M_1/R phase VO_2 nanobundles were obtained through heat-transformation from $VO_2(B)$. Structural characterization indicated that these VO_2 nanobundles are assembled by a large number of nanowires, and $VO_2(M_1/R)$ nanobundles have better crystallinity after heat-transformation. Their temperature-dependent FE measurement indicated that FE properties of these two phases of nanobundles can both be improved by increasing the ambient temperature. Moreover, for the $VO_2(M_1/R)$ nanobundles, their FE properties are also strongly dependent on the MIT process, and about a three-orders-of-magnitude increasing of the emission current density has been observed in this process at an applied field of 6 V/μm. These characteristics make $VO_2(M_1/R)$ a promising material for new type of temperature-controlled field emitters whose emission density can be adjusted by ambient temperature rather than applied field.

AUTHOR INFORMATION

Corresponding Author
*E-mail: yk5188@263.net.

ACKNOWLEDGMENT

The authors acknowledge financial support from the NSF of China (Grant 60976014, 60976004, and 11074075), the Key Basic Research Project of Scientific and Technology Committee of Shanghai (Grant 09DJ1400200) and the Program for Changjiang Scholars and Innovative Research Team in University (PCSIRT). The author H. Yin acknowledges Kemin Jiang and Ningbo Institute of Material Technology and Engineering of Chinese Academy of Sciences for the UPS measurement.

REFERENCES

(1) Rinzler, A. G.; Hafner, J. H.; Nikolaev, P.; Lou, L.; Kim, S. G.; Tomanek, D.; Nordlander, P.; Colbert, D. T.; Smalley, R. E. *Science* **1995**, *269*, 1550.
(2) De Heer, W. A.; Ugarte, D. *Science* **1995**, *270*, 1179.
(3) Lee, C. J.; Lee, T. J.; Lyu, S. C.; Zhang, Y. *Appl. Phys. Lett.* **2002**, *81*, 3648.
(4) Wan, Q.; Yu, K.; Wang, T. H.; Lin, C. L. *Appl. Phys. Lett.* **2003**, *83*, 2253.
(5) Banerjee, D.; Jo, S. H.; Ren, Z. F. *Adv. Mater.* **2004**, *16*, 2028.
(6) Dai, Z. R.; Pan, Z. W.; Wang, Z. L. *Adv. Funct. Mater.* **2003**, *13*, 9.
(7) Jia, H.; Zhang, Y.; Chen, X.; Shu, J.; Luo, X.; Zhang, Z.; Yu, D. *Appl. Phys. Lett.* **2003**, *82*, 4146.
(8) Chen, J.; Deng, S. Z.; Xu, N. S.; Zhang, W. X.; Wen, X. G.; Yang, S. H. *Appl. Phys. Lett.* **2003**, *83*, 746.
(9) Miyauchi, M.; Tokudome, H.; Toda, Y.; Kamiya, T.; Hosono, H. *Appl. Phys. Lett.* **2006**, *89*, 043114.
(10) Wu, M. S.; Lee, J. T.; Wang, Y. Y.; Wan, C. C. *J. Phys. Chem. B* **2004**, *108*, 16331.
(11) Li, Y. B.; Bando, Y.; Golberg, D. *Adv. Mater.* **2003**, *15*, 1294.
(12) Liu, J. G.; Zhang, Z. J.; Zhao, Y.; Su, X.; Liu, S.; Wang, E. G. *Small* **2005**, *1*, 310.
(13) Leroux, C.; Nihoul, G.; Tendeloo, G. V. *Phys. Rev. B* **1998**, *57*, 5111.
(14) Hagrman, D.; Zubieta, J.; Warren, C. J.; Meyer, L. M.; Treacy, M. M. J.; Haushalter, R. C. *J. Solid State Chem.* **1998**, *138*, 178.
(15) Morin, F. J. *Phys. Rev. Lett.* **1959**, *3*, 34.
(16) Chen, C.; Zhou, Z. *Appl. Phys. Lett.* **2007**, *91*, 011107.
(17) Driscoll, T.; Kim, H. T.; Chae, B. G.; Ventra, M. D.; Basov, D. N. *Appl. Phys. Lett.* **2009**, *95*, 043503.
(18) Driscoll, T.; Kim, H. T.; Chae, B. G.; Kim, B. J.; Lee, Y. W.; Jokerst, N. M.; Palit, S.; Smith, D. R.; Ventra, M. D.; Basov, D. N. *Science* **2009**, *325*, 1518.
(19) Li, W.; Dahn, J. R.; Wainwright, D. S. *Science* **1994**, *264*, 1115.
(20) Tsang, C.; Manthiram, A. *J. Electrochem. Soc.* **1997**, *144*, 520.
(21) Gui, Z.; Fan, R.; Mo, W. Q.; Chen, X. H.; Yang, L.; Zhang, S. Y.; Hu, Y.; Wang, Z. Z.; Fan, W. C. *Chem. Mater.* **2002**, *14*, 5053.
(22) Baudrin, E.; Sudant, G.; Larcher, D.; Dunn, B.; Tarascon, J. M. *Chem. Mater.* **2006**, *18*, 4369.
(23) Wang, Y. Q.; Zhang, Z. J. *Physica E* **2009**, *41*, 548.
(24) Liao, L.; Zhang, W. F.; Lu, H. B.; Li, J. C.; Wang, D. F.; Liu, C.; Fu, D. J. *Nanotechnology* **2007**, *18*, 225703.
(25) Liebsch, A.; Ishida, H.; Bihlmayer, G. *Phys. Rev. B* **2005**, *71*, 085109.
(26) Yao, T.; Zhang, X. D.; Sun, Z. H.; Liu, S. J.; Huang, Y. Y.; Xie, Y.; Wu, C. Z.; Yuan, X.; Zhang, W. Q.; Wu, Z. Y.; Pan, G. Q.; Hu, F. C.; Wu, L. H.; Liu, Q. H.; Wei, S. Q. *Phys. Rev. Lett.* **2010**, *105*, 226405.
(27) Sakuma, R.; Miyake, T.; Aryasetiawan, F. *Phys. Rev. B* **2008**, *78*, 075106.
(28) Koethe, T. C.; Hu, Z.; Haverkort, M. W.; Schüssler-Langeheine, C.; Venturini, F.; Brookes, N. B.; Tjernberg, O.; Reichelt, W.; Hsieh, H. H.; Lin, H. J.; Chen, C. T.; Tjeng, L. H. *Phys. Rev. Lett.* **2006**, *97*, 116402.
(29) Biermann, S.; Poteryaev, A.; Lichtenstein, A.; Georges, A. *Phys. Rev. Lett.* **2005**, *94*, 026404.